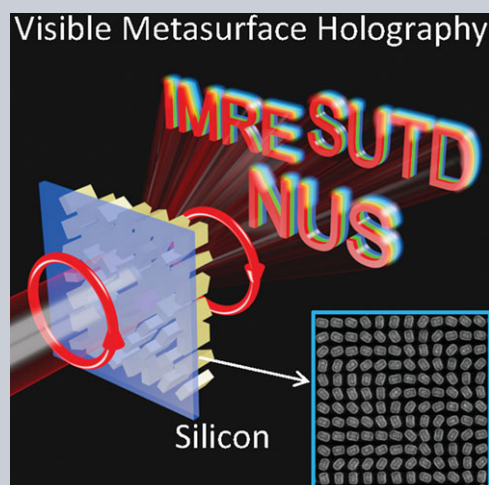


Abstract The dielectric metasurface hologram promises higher efficiencies due to lower absorption than its plasmonic counterpart. However, it has only been used, up to now, for controlling linear-polarization photons to form single-plane holographic images in the near-infrared region. Here, we report a transmission-type metahologram achieving images in three colors, free from high-order diffraction and twin-image issues, with 8-level modulation of geometric phase by controlling photon spin via precisely patterned Si nanostructures with varying orientations. The resulting real and virtual holographic images with spin dependence of incident photons natively enable the spin degeneracy removal of light, leading to a metahologram-enabled spin Hall effect of light. Low-absorption dielectrics also enable us to create holograms for short-wavelength light down to 480 nm, thus spanning the three primary colors. It possesses the potential for compact color-display chips using mature semiconductor processes, and holds significant advantages over previous metaholograms operating at longer wavelengths.



Silicon multi-meta-holograms for the broadband visible light

Kun Huang^{1,2,**}, Zhaogang Dong^{2,**}, Shengtao Mei^{1,3,**}, Lei Zhang¹, Yanjun Liu², Hong Liu², Haibin Zhu⁴, Jinghua Teng², Boris Luk'yanchuk⁵, Joel K.W. Yang^{6,2,*}, and Cheng-Wei Qiu^{1,3,*}

1. Introduction

Recently, metasurfaces [1], consisting of ultrathin metallic nanostructures, have shown great promise in the full control of the polarization, amplitude and phase of light [2]. The resulting applications include high-efficiency plasmonic couplers [3], aberration-free [4] and dual-polarity [5] metalenses, compact vortex generators [6–8], novel metaholograms [9–19], optical nonlinear signal generation [20] and manipulation [21]. Among them, the metasurface hologram is arguably the most intriguing one because it has advantages in providing large space–bandwidth product as well as in eliminating high-order diffraction and twin images [9–12] than traditional holograms, leading to numerous applications [22–28].

Currently, a high-efficiency plasmonic metasurface hologram is implemented in reflective mode with a record efficiency of ~80% in the near-infrared regime [12]. Meanwhile, plasmonic metasurface holograms, working in transmission mode, still suffer from low efficiencies due to Ohmic losses in metals. Nevertheless, transmission-mode components are equally important as many optical systems

and elements operate in transmission mode across the infrared, visible, X-ray [29] and even relativistic electrons [30], without the native challenge in separating the reflected signal from the incident one. Moreover, one potential approach to achieve a high-efficiency transmission hologram is to adopt high-index dielectrics, e.g. silicon [31] and TiO₂ [32], which have much lower extinction coefficients than metals in the visible to infrared regime. At the point of writing, the dielectric metahologram has only demonstrated the control of light with linear polarization in the near-infrared regime [33]. Furthermore, in the visible region, transmission metaholograms based on metals suffer from low efficiency, single-wavelength or the narrow bandwidth operation in the long-wavelength range of the visible spectrum [9–11]. Therefore, dielectric metaholograms in the entire visible spectrum are greatly desirable in applications such as multicolor holographic displays, and high-security image encryption.

On the other hand, spin photonics [34] as an emerging field has gained much attention by developing various nanophotonics devices to manipulate spin photons for applications, such as chirality-distinguishing beam splitters

¹ Department of Electrical and Computer Engineering, National University of Singapore, 4 Engineering Drive 3, Singapore 117583, Singapore

² Institute of Materials Research and Engineering, Agency for Science, Technology and Research (A*STAR), 2 Fusionopolis Way, Innovis, #08-03, Singapore 138634, Singapore

³ NUS Graduate School for Integrative Sciences and Engineering, National University of Singapore, 28 Medical Drive, Singapore 117456

⁴ College of Mechanical and Electrical Engineering, Jiaxing University, Jiaxing 314001, China

⁵ Data Storage Institute, Agency for Science, Technology and Research (A*STAR), 2 Fusionopolis Way, Innovis, #08-01, Singapore 138634, Singapore

⁶ Singapore University of Technology and Design, 8 Somapah Road, Singapore 487372

**These authors contributed equally to this work

*Corresponding author: C.-W. Q. e-mail: eleqc@nus.edu.sg or J.K.W.Y. e-mail: joel_yang@sutd.edu.sg

[35], the spin Hall effect (SHE) of light [36], spin-dependent metalenses [5] and couplers of surface plasmon polaritons [37]. It mainly focuses on the inverse behavior of spin light for removing optical spin degeneracy [34], which can be realized more easily with the help of a spin-sensitive meta-hologram due to its powerful capability in the complex manipulation of light. The combination of spin photonics and metahologram could significantly simplify the experimental observation of spin splitting of light without the requirement of rigorous circumstances [38] or complicated designs [34, 36, 39].

In this paper, we demonstrate a novel Si metasurface hologram that manipulates the spin of light in the visible (instead of infrared) wavelengths. This metahologram, composed of position-varying silicon nanorods, exhibits multicolor holographic images without high-order diffraction and twin-image issues at multiple z -planes. By lithographic patterning, the orientation of silicon nanorods was varied as a function of position to provide the required phase modulation for the transmitted spin-inversed photons. Due to the excitation of magnetic resonances and lower absorption coefficient compared to metals, these subwavelength silicon nanorods are able to function as nanoscopic dispersion-less half-waveplates from 480 nm to 680 nm. Bringing metaholograms into the visible spectrum crucially enables their application in imaging and displays. In addition, detailed numerical and experimental results show that employing single-crystal silicon and tuning the geometry of silicon nanorods should improve the holographic quality further, which provides an instructive guide for high-efficiency manipulation of light by dielectric metaholograms.

2. Materials and methods

Stemming from the different responses to the transverse electric and magnetic fields of incident light, individual nanorods with a large aspect ratio, i.e. length (l) / width (w), exhibit significant birefringence, which can be utilized to control the spin of photons [40]. Our optimized structure with $l = 190$ nm, $w = 100$ nm and $h = 370$ nm is equivalent to a miniaturized half-waveplate that reverses the spin of the photon (Fig. 1a) and imprints the spin-inversed photons with a geometric phase, depending on the orientation of the nanorod [35]. Although metallic nanorods can also work as miniaturized half-waveplates with the help of plasmon resonances [40, 41], our silicon nanorod possesses a different underlying physics of employing magnetic resonance, which will be shown later.

The geometric phase of the transmitted photons with inversed spins, induced by a silicon nanorod, only depends on its orientation angle θ as denoted in Fig. 1b and shows the dispersion-less characteristic. The transfer efficiency η_{TR} , defined as the ratio between the power of transmitted spin-inversed photons to that of incident photons, is a function of the illumination wavelength. Therefore, the Jones matrix of a silicon nanorod with a rotating angle θ can be expressed as

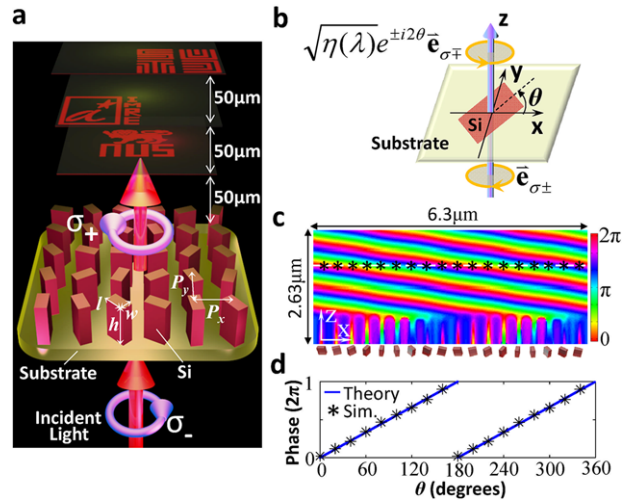


Figure 1 Mechanism of three-dimensional holography via silicon metasurface. (A) Sketch of manipulating spin photons via silicon nanorod array for reconstructing three holographic images at three separate planes $50\mu\text{m}$, $100\mu\text{m}$ and $150\mu\text{m}$ away from the sample. The silicon nanorod has a geometry of length $l = 190$ nm, width $w = 100$ nm and height $h = 370$ nm. This hologram has a pixel pitch of $P_x \times P_y = 350 \text{ nm} \times 350 \text{ nm}$. (B) Transmission of spin photons through a silicon nanorod with an orientation angle of θ . The transmitted photons with inversed spins are imprinted with a geometrical phase of $e^{\pm 2i\theta}$. (C) Phase profile of transmitted photons with inversed spins through a periodic array with θ varying (from 0° to 340° with an equal interval of 20°) silicon nanorods along x in one period. The phase profile from $z = 0$ (where the top surface of the nanorod is located) to $z = 2.63 \mu\text{m}$ shows a tilting phase profile, implying that the light is imprinted with a gradient phase by θ -varying silicon nanorods. The simulated phase data labeled by black asterisks (whose x coordinates are the same with those of nanorod) at $z = 1.84 \mu\text{m}$ (dashed white line) is chosen as an example to compare with the theoretical prediction as shown by the blue line in (D).

$$\begin{aligned} \mathbf{T}(\theta) &= \mathbf{R}(-\theta) \mathbf{T}_0 \mathbf{R}(\theta) = \begin{bmatrix} \cos\theta & -\sin\theta \\ \sin\theta & \cos\theta \end{bmatrix} \\ &= \begin{bmatrix} i\sqrt{\eta_{\text{TR}}}(\lambda) & 0 \\ 0 & -i\sqrt{\eta_{\text{TR}}}(\lambda) \end{bmatrix} \begin{bmatrix} \cos\theta & \sin\theta \\ -\sin\theta & \cos\theta \end{bmatrix} \\ &= i\sqrt{\eta_{\text{TR}}}(\lambda) \begin{bmatrix} \cos 2\theta & \sin 2\theta \\ \sin 2\theta & -\cos 2\theta \end{bmatrix}, \end{aligned} \quad (1)$$

where $\mathbf{R}(\theta)$ is the rotation operator and \mathbf{T}_0 is the Jones matrix of the silicon nanorod without rotation. With the right- and left-handed spins of incident light are labeled σ_{\pm} with Jones vectors $[1, \pm i]^T$ (superscript T denotes matrix transposition), one can easily obtain its transmitted electric field

$$\mathbf{E}_{\text{trans}} = \mathbf{T}(\theta) \begin{bmatrix} 1 \\ \pm i \end{bmatrix} = i\sqrt{\eta_{\text{TR}}}(\lambda) e^{\pm 2i\theta} \begin{bmatrix} 1 \\ \mp i \end{bmatrix}, \quad (2)$$

where the $e^{\pm 2i\theta}$ is the dispersion-less geometric phase, and the spin of the transmitted photon is flipped from “ σ_{\pm} ”

to “ σ_{\mp} ”. It is worth noting that Eq. (2) is only valid for transmitted photons with inverse spins as evaluated by its transfer efficiency η_{TR} , which determines the total optical efficiency of the metahologram. The transfer efficiency η_{TR} depends on the absorption coefficient and the geometry of the silicon nanorod.

Significantly, the geometric phase in Eq. (2) shows a linear dependence on the orientation angle of nanorods with a factor of 2, which greatly reduces the design complexity. To verify such a linear dependence, numerical simulations were carried out by using a finite-domain time-difference (FDTD) method (Lumerical), where periodic boundary conditions were used along x - and y -axes, with a perfect-matched layer (PML) along the z -axis. A series of silicon nanorods, with the orientation angles increasing from 0° to 340° with a step of 20° , was illuminated by a plane wave at 633 nm with a spin of σ_{+} . The transmitted light has the inverse spin of σ_{-} with a tilting wavefront as shown in Fig. 1c, indicating a gradient phase modulation by nanorods. Figure 1d presents a quantitative comparison between the theoretical prediction with Eq. (2) and the simulated phase values at a z -cut plane (dashed line in Fig. 1c), which is $1.84\ \mu\text{m}$ away from the sample surface, showing an excellent agreement. This means that one can conveniently control the phase of transmitted spin-inversed photons as a function of space by controlling the orientation and position of the nanorod to realize a multilevel phase modulation for reconstructing holographic images.

Compared to a binary hologram, the multilevel phase modulation in our hologram is capable of reconstructing distinct images at different z -cut planes. Here, we demonstrate the 3-dimensional holographic reconstruction in the Fresnel region, where the propagation of light is approximated by the Fresnel diffraction theory as solved by a chirp-transform method for fast simulation [27, 42]. To obtain the expected phase profile, a modified Gerchberg–Saxton algorithm [43] is employed based on a phase-feedback strategy, which rests on the basis of a weight superposition of every phase profile for its individual holographic image. The weight coefficient is evaluated by the root-mean-square (RMS) error between the ideal and real images in the last iteration (see Section 1 in Supporting Information). For three-dimensional holography in Fig. 1a, 1000 iterations were carried out to retrieve its phase profile with a pupil diameter of $120\ \mu\text{m}$ and a pixel size of $350\text{ nm} \times 350\text{ nm}$ (as shown in Fig. 2a), realizing three reconstructed images of “NUS”, “IMRE” and “SUTD”, i.e., the abbreviations of the three affiliations of the authors, at the z -planes of $z = 50\ \mu\text{m}$, $100\ \mu\text{m}$ and $150\ \mu\text{m}$, respectively.

Under the configuration of rotated silicon nanorods, we encode the phase profile $P(x_0, y_0)$ of the hologram in Fig. 2a into a nanorod array with their orientation angles θ obeying Eq. (2). Here, an 8-level phase modulation is employed as exhibited in Fig. 2b. Assuming that the incident light has the electric field $\mathbf{E}_{\text{in}}^{\sigma_{\pm}} = A(x_0, y_0)[1, \pm i]^T$, where its amplitude $A(x_0, y_0)$ is taken as unity for uniform illumination here. We show that the spin-inversed light transmitted through this silicon hologram has the diffraction field

in Fresnel region as

$$\begin{aligned} \mathbf{E}_{\text{trans}}^{\sigma_{\mp}}(x, y, z) &= \text{FresnelT} \left\{ \sqrt{\eta_{TR}(\lambda)} A(x_0, y_0) e^{\pm i P(x_0, y_0)} \begin{bmatrix} 1 \\ \mp i \end{bmatrix} \right\} \\ &= \frac{\exp(i2\pi z/\lambda)}{i\lambda z} \iint_{-\infty}^{\infty} \sqrt{\eta_{TR}(\lambda)} A(x_0, y_0) e^{\pm i P(x_0, y_0)} \begin{bmatrix} 1 \\ \mp i \end{bmatrix} \\ &\quad \cdot \exp \left\{ i \frac{\pi}{\lambda z} [(x - x_0)^2 + (y - y_0)^2] \right\} dx_0 dy_0, \quad (3) \end{aligned}$$

where $\text{FresnelT}\{\}$ means the propagation of light in the Fresnel region. The sign “ \pm ” of $e^{\pm i P(x_0, y_0)}$ depends on the spin of the incident light, where it leads to the real and virtual holographic images with convergent and divergent waves, respectively. Such a capability of a metahologram in polarization control of light will be verified experimentally later.

Due to the dispersion-less phase profile $P(x_0, y_0)$ realized by our silicon hologram, the integral result in Eq. (3) remains mathematically identical at different wavelengths under the rigorous condition of $\lambda_1 z_1 = \lambda_2 z_2$. In other words, one holographic image will be reconstructed without any scaling (i.e., x and y are the same for different wavelengths) at a series of z -planes as obeying this straightforward dispersion relationship. Note that this dispersion relationship rigorously demonstrates the capability of our metahologram for achieving broadband operation of visible light, as numerically verified in Fig. S1 of Supporting Information. Therefore, due to the significant difference from a traditional hologram in the engineering realization of the phase profile, our proposed metahologram is competent at both polarization control and broadband operation of light. In comparison, traditional holograms based on propagation-accumulated phase delay in low-index dielectrics, such as quartz [27] and a spatial light modulator [44], are wavelength dependent so that their corresponding holographic images will disappear when the wavelength of the illumination light is different from the designed one.

The designed metahologram is fabricated on a 370-nm thick amorphous silicon film as deposited onto a $500\text{-}\mu\text{m}$ thick glass substrate via electron-beam lithography (ELS-7000, Elionix) followed by dry etching of the silicon [45]. The detailed processes and conditions are shown in Section 2 of Supporting Information. Figure 2c presents the scanning electron micrograph (SEM) image of the fabricated silicon hologram with a gradually varying orientation of nanorods. Its optical characterization was done using a modified photon scanning tunnelling microscope (Alpha 300S, WITec GmbH) in a confocal configuration, as shown in Fig. 2d. After collimated by a lens L_1 , a laser beam from a fiber is illuminated onto the sample that is fixed on a high-precision 3-axis positioning stage. The circularly polarized light source is generated by passing the collimated light through a circular polarizer, which consists of a linear polarizer LP_1 and a quarter waveplate

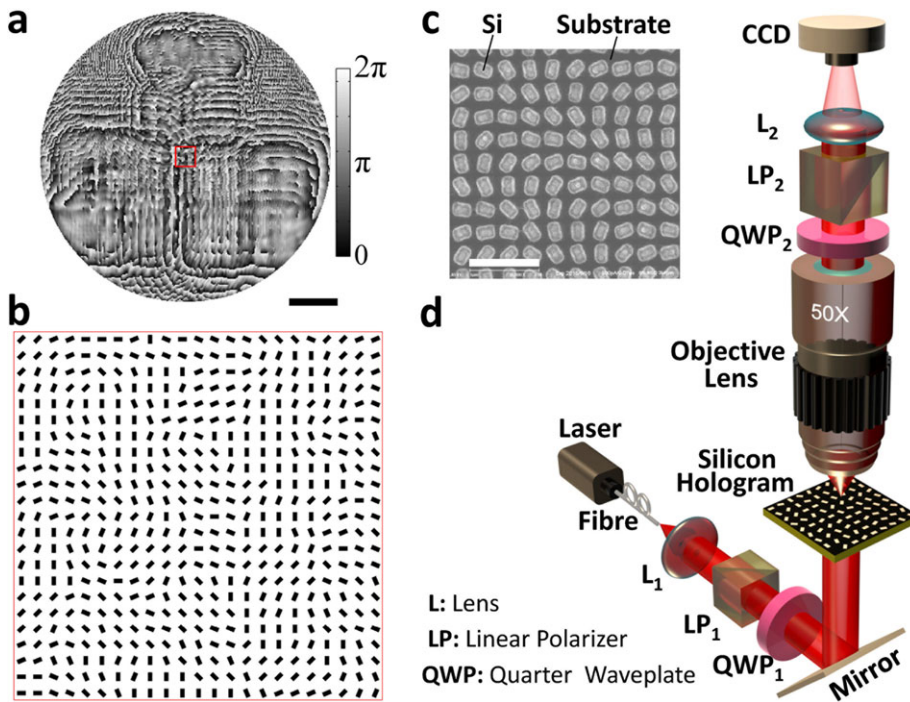


Figure 2 Demonstration of three-dimensional metahologram. (A) Designed phase profile for three-dimensional hologram with its diameter of $120\ \mu\text{m}$. Scale bar, $20\ \mu\text{m}$. (B) Sketch of silicon nanorod (black rectangles) array encoding designed phase of hologram (encircled in red rectangle of (a)). (C) SEM image of one part of fabricated silicon metahologram consisting of 92,361 nanorods. Scale bar, $1\ \mu\text{m}$. (D) Experimental setup for characterizing the hologram.

QWP₁. The holographic images as formed by transmitted spin-inversed photons is collected by a $\times 50$ objective lens and filtered by another circular-polarization analyzer, before projecting onto a charge-coupled device (CCD) via a lens L₂.

3. Results and discussions

Figure 3 shows the experimentally captured holographic images at three z -planes with a spin dependence of incident photons. When incident photons have right-handed spins, the transmitted photons with left-handed spins will be used to reconstruct three convergent images labeled “NUS”, “IMRE” and “SUTD” at $z = 50\ \mu\text{m}$, $100\ \mu\text{m}$ and $150\ \mu\text{m}$, respectively, in Fig. 3a. In comparison, for incident photons with left-handed spins, its transmitted photons will be imprinted with divergent wavefronts as shown in Fig. 3b, where three virtual holographic images can be observed at $z = -50\ \mu\text{m}$, $-100\ \mu\text{m}$ and $-150\ \mu\text{m}$, by changing the sample–objective distance in the opposite direction (as denoted by the sign ‘-’ for distinction). It is worthy to note that both real and virtual holographic images nearly have the same distribution without any significant distortion, as predicted in Eq. (3), demonstrating its capability of manipulating spin light in three-dimensional space. Interestingly, this spatial splitting of holographic images for two spins of incidence unveils the spin degeneracy removal of photons, indicating metahologram-enabled SHE of light.

In addition, because the oriented nanorod can easily realize multiple levels of phase modulation, our metaholo-

gram can achieve extremely high diffraction efficiency η_{DE} , which is defined by the ratio between the total intensity of three images to that of transmitted light with inversed spins (see Fig. S2 in Supporting Information). In our experiment, the measured η_{DE} is 75% at 633 nm. The total optical efficiency $\eta = \eta_{\text{TR}} \cdot \eta_{\text{DE}}$ (defined by the ratio of the total intensity of three images to the incident intensity) is measured $\sim 3\%$ at 633 nm, which is likely limited by the amorphous state of our silicon, as discussed latter.

To confirm the broadband operation of our silicon hologram, a supercontinuum laser is used as the illumination light with selected wavelengths from $\lambda = 480\ \text{nm}$ to $\lambda = 680\ \text{nm}$. The captured holographic images and the measured dispersion relationship are shown in Fig. 4. Distinguishable images can be observed especially for $\lambda > 580\ \text{nm}$, although the image-quality parameters such as uniformity, shape and background noise vary slightly with illuminating wavelengths in the experiment. We would like to emphasize that, although the previous metallic metahologram in transmission mode has shown broadband operation in three-dimensional holography [11], its reported operating wavelength is larger than 670 nm, due to the much larger absorption coefficient of metal than silicon at shorter wavelengths in transmission mode. In comparison, metaholograms, with supercell pixels and feature size larger than one wavelength, have been reported to be capable of operating at shorter wavelengths, e.g., 405 nm [13, 14, 16]. However, they suffer from high-order diffraction and twin images like traditional holograms. The use of a subwavelength pitch design makes our proposed metahologram immune to these two problems. Therefore, to the best of our knowledge, our

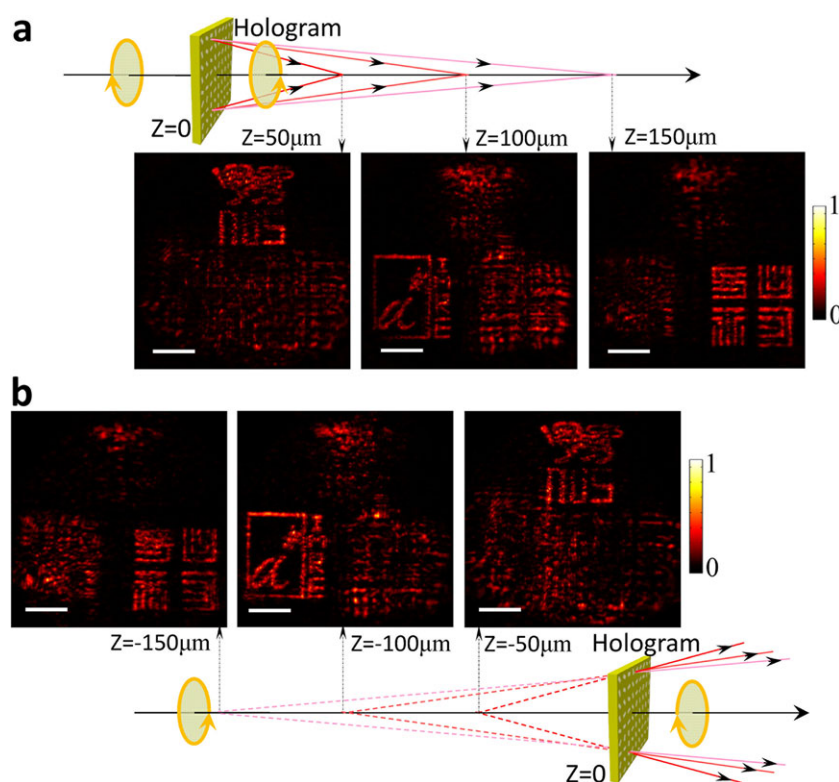


Figure 3 Measured three-dimensional holographic images. Captured holographic images with different x , y and z coordinates under the illuminating light with left- (A) and right- (B) handed spins. The transmitted light with inversed spins has the convergent (A) and divergent (B) wavefronts for holographic images. Scale bar, $20 \mu\text{m}$.

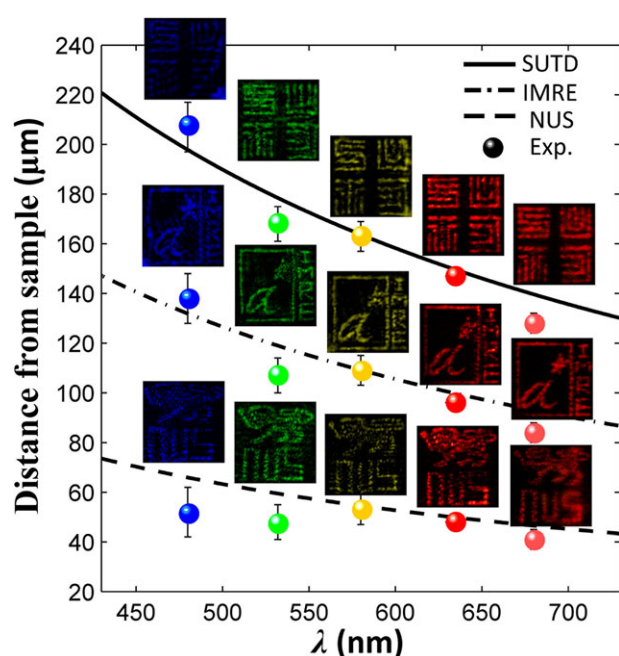


Figure 4 Broadband operation of silicon metahologram. The theoretical (curves) and experimental (dots) dispersion relationships are provided by the distance between the sample and the z -position of every holographic image as a function of wavelength λ . Insets: the experimental holographic images are provided with different wavelengths of 480 nm, 532 nm, 580 nm, 633 nm and 680 nm, showing a better image quality for $\lambda > 580$ nm.

silicon metahologram is the first attempt to realize the challenging broadband operation (i.e., spectrum width of 200 nm) of visible light with short wavelengths in transmission mode (more details are given in Table 1), which paves a critical step towards the application of metaholograms in displays.

Although the metahologram has very good simulation performance, as shown in the insets of Fig. S1, we have also observed that the experimentally measured holographic quality has a tight dependence on illumination wavelength in Fig. 4. This discrepancy is mainly caused by the fact that the transmitted or reflected light of a metasurface contains two parts. One is “signal light” with crosspolarization (orthogonal to incident polarization) with the modulated phase by metasurface. The other one is “noise light” having the same polarization as the incident one without any phase modulation and it will destroy the image quality due to its unwanted interference with “signal light”, if it is not completely filtered out in an experiment.

From the viewpoint of experiment, we here make a detailed investigation about the factors determining image quality of nanorod metahologram. Without loss of generality, we assume that the polarization analyzer (i.e., QWP₂ and LP₂ in Fig. 2d) has no spatial volume so that it could be inserted immediately after the silicon-hologram sample. Thus, light after passing through the silicon hologram and this polarization analyzer has the diffracting field

Table 1 A comparison between our silicon hologram and other reported metaholograms. In order to give a clear demonstration of our hologram, we provide a detailed comparison between our metahologram and other reported holograms in optical efficiency, operating wavelength, twin-image and high-order diffraction issues in Table 1. It clearly shows that the performance of reflective metaholograms has been improved very rapidly after 2015, especially in enhancing optical efficiency, eliminating high-order diffraction and twin-image issues. However, for transmissive metaholograms, the good performance is only shown in the infrared region. The broadband operation in short-wavelength visible light is very challenging in a transmitted mode, while it is realized by our silicon hologram with a bandwidth of 200 nm from blue to red light. Therefore, our hologram is the first one to realize the broadband operation of visible light among all transmissive metaholograms. Although our efficiency is not high enough due to the amorphous silicon, it has the great potential in enhancing the efficiency through crystallized silicon as demonstrated in this paper

Operating mode	Literature	Total efficiency	Wavelength	Twin image	High-order diffraction	Materials
Reflection	Butt et al. (2012) [50]	Not reported	454 nm, 532 nm, 635 nm	Yes	Yes	Carbon nanotube
	Huang et al. (2015) [13]	0.64–0.69%	405 nm, 532 nm, 658 nm	Yes	Yes	Aluminum
	Montelogo et al. (2013) [17]	3%	650 nm	Yes	Yes	Silver
	Montelongo et al. (2014). [16]	3%	405 nm, 650 nm	Yes	Yes	Silver
	Chen et al. (2013) [14]	18%	405 nm, 633 nm, 780 nm	Yes	Yes	Gold
	Wen et al. (2015) [19]	40%	475–1100 nm	No	No	Silver
	Yifat et al. (2014) [51]	60%	1550 nm	Yes	No	Gold
	Zheng et al. (2015) [12]	80%	600–1100 nm	No	No	Gold
	Transmission	Huang et al. (2013) [11]	Not reported	670–950 nm	No	No
Walther et al. (2012) [15]		0.1%	905 nm, 1385 nm	Yes	Yes	Gold
Zhou et al. (2013) [52]		0.2%	1550 nm	Not reported	Not reported	Gold
Huang et al. (2015) [9]		2%	532 nm	No	No	Chromium
Ni et al. (2013) [10]		10%	676 nm	No	No	Gold
Arbabi et al. (2015) [33]		84–91%	915 nm	No	No	Silicon
Our hologram		3%	480–680 nm	No	No	Silicon

$$\begin{aligned}
 \mathbf{E}_{\text{trans}} &= \mathbf{E}_{\text{trans}}^{\sigma\mp}(x, y, z) + \mathbf{E}_{\text{trans}}^{\prime\sigma\pm}(x, y, z) \\
 &= \text{FresnelT} \left\{ \sqrt{\eta_{\text{TR}}(\lambda)} A(x_0, y_0) e^{\pm i P(x_0, y_0)} \begin{bmatrix} 1 \\ \mp i \end{bmatrix} + \sqrt{\beta} \cdot \sqrt{\gamma(\lambda)} \cdot A(x_0, y_0) \begin{bmatrix} 1 \\ \pm i \end{bmatrix} \right\} \\
 &= \sqrt{\eta_{\text{TR}}(\lambda)} \text{FresnelT} \left\{ A(x_0, y_0) \cdot \left((e^{\pm i P(x_0, y_0)} + c) \begin{bmatrix} 1 \\ 0 \end{bmatrix} + (e^{\pm i P(x_0, y_0)} - c) \begin{bmatrix} 0 \\ \mp i \end{bmatrix} \right) \right\}, \quad (4)
 \end{aligned}$$

where $\mathbf{E}_{\text{trans}}^{\prime\sigma\pm}(x, y, z)$ stands for the noise light after the polarization analyzer. $\gamma(\lambda)$ is the ratio of the intensity of noise light to the incident intensity of metahologram. The attenuation parameter β of polarization analyzer is defined by the ratio between its minimum transmitted intensity to the incident intensity of analyzer and the relative noise $c = \sqrt{\gamma\beta}/\eta_{\text{TR}}$ determines the image quality. Here, we would like to emphasize that Eq. (4) is another important result in this paper, which is valid for all metasurface-based devices and gives a complete description of all possible holographic images obtained experimentally. To evaluate the effect of relative noise c in experiment, we calculate their RMS error between predicted images by Eq. (4) and the ideal ones in

Fig. 5a. This indicates that the holographic images dominate the target plane without significant background noise if the relative noise c is below 2 (or $\eta_{\text{TR}}/\gamma > 4/\beta$). Considering that β is generally fixed in an experiment, it is more important to increase the ratio η_{TR}/γ rather than η_{TR} in improving the experimental quality of holographic images. In addition, it also predicts that a high-quality holographic image is still achievable in experiment even if η_{TR} is every low, which is significantly distinct from the view that high-quality holography usually requires high transfer efficiency η_{TR} .

An experimental investigation on η_{TR} and η_{TR}/γ is implemented to verify the above prediction by illuminating a

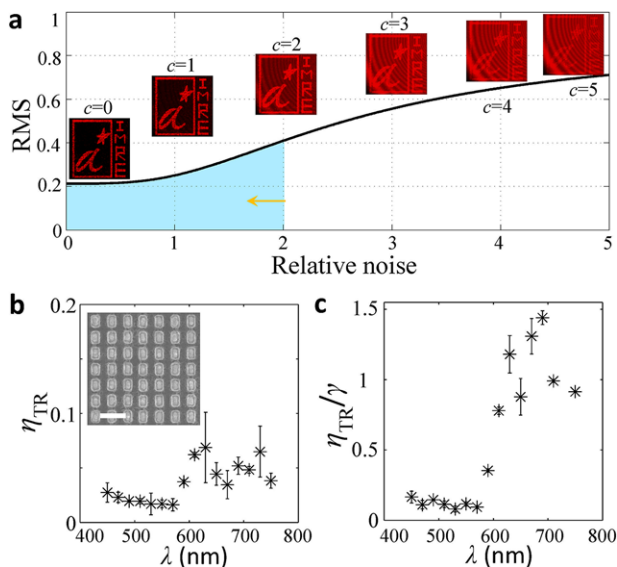


Figure 5 Evaluation of holographic quality. (A) The RMS error between real and ideal images at different relative-noise of c defined in Eq. (4). The calculation of RMS error is implemented by using holographic image “IMRE” in a spatial range of interest, i.e., $42 \mu\text{m} \times 42 \mu\text{m}$. Insets: The calculated holographic images from $c = 0$ to $c = 5$ with a gradually increased background. (B) Measured transfer efficiency η_{TR} for a periodic array of our silicon nanorod. Inset: SEM images of silicon nanorod array. Scale bar, 500 nm. (C) Measured ratio η_{TR}/γ of the same periodic array. It shows a rapid increment for $\lambda > 580$ nm, being consistent with high-quality images in Fig. 4.

350-nm period array of the proposed silicon nanorods by a supercontinuum laser with wavelength ranging from 450 nm to 750 nm. Figure 5b shows the wavelength-dependent transfer efficiency η_{TR} of around 5% obtained experimentally, with which it is difficult to predict its holographic quality. However, the measured ratio η_{TR}/γ has an abrupt increment for $\lambda > 580$ nm, indicating a better image quality than that for $\lambda < 580$ nm. This shows a good agreement with the experimental results in Fig. 4 and confirms the validity of predictions by Eq. (4).

Next, we investigate the approaches of decreasing the relative noise c . Because the quarter-waveplate and linear polarizer in a circular-polarization analyzer are commercially achievable, its attenuation parameter β is taken to be fixed and its role is ignored in the following discussions. Thus, we only consider the possible methods by increasing the ratio η_{TR}/γ , which tightly depends on the material properties and nanorod’s geometry. First, the extinction coefficients of materials should be as small as possible to minimize the ohmic loss. We give a detailed comparison between their extinction coefficients of gold (Palik), crystalline silicon (c-silicon, Palik) and our amorphous silicon (a-silicon) in Fig. 6a. The extinction coefficient of a-silicon, measured by an ellipsometer, is much smaller than that of gold, for which we are able to push its operating wavelength down to 480 nm, as demonstrated above. However, a-silicon shows stronger absorption than c-silicon, which

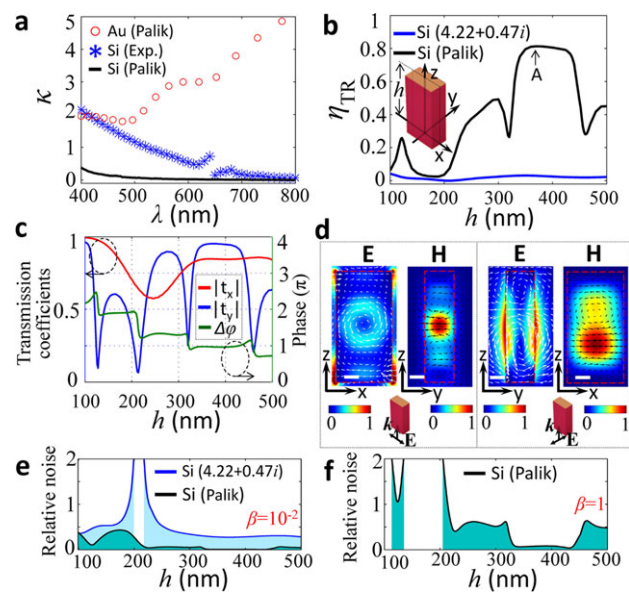


Figure 6 Factors determining holographic quality. (A) Extinction coefficients of Au (Palik, red hollow circles), Si (Palik, solid black curve) and our amorphous Si (blue asterisks, measured by an ellipsometer). (B) Transfer efficiency η_{TR} of crystalline (Palik, black curve) and amorphous (blue curve, with measured refractive index of $4.22+0.47i$) silicon at $\lambda = 633$ nm as a function of nanorod height h ranging from 100 nm to 500 nm. The width and length of nanorod is fixed at $w = 100$ nm and $l = 190$ nm in our paper. Point A is pointing to the peak and valley transfer efficiency of crystalline silicon with $h = 370$ nm. Insets: The three-dimensional coordinate used in all simulations of this paper. (C) The transmission of crystalline silicon nanorod under the x - and y -polarized illumination. Their individual transmission coefficients are t_x and t_y with a phase difference of $\Delta\varphi = \text{Arg}\langle t_x \rangle - \text{Arg}\langle t_y \rangle$, where $\text{Arg}\langle \cdot \rangle$ is the argument of a complex number. (D) The cross-section intensity and vector profiles of electric (**E**) and magnetic (**H**) fields in silicon nanorod (red dashed rectangles) of Point A ($h = 370$ nm) in (b) under the x - (left) and y - (right) polarized illumination. The white and black arrows denote vector direction of **E** and **H**, respectively. Insets: The wave vector (**k**) and polarization (**E**) of incident light for both illuminations. Scale bar, 50 nm. (E) The relative noise c of crystalline (black curve) and amorphous (blue curve) silicon for a polarization analyzer’s attenuation parameter $\beta = 10^{-2}$. For amorphous silicon, its relative noise c is larger than 2 around $h = 200$ nm, implying a poor image quality. (F) The relative-noise c of crystalline (Palik) silicon without employing any polarization analyzer, i.e., $\beta = 1$. This shows that the holographic quality is also good for height h located in the color region.

provides an opportunity to improve the holographic quality further.

Secondly, the geometry of silicon nanorod is also important to tune the electric and magnetic resonance in silicon for a high ratio η_{TR}/γ . Considering that the large aspect ratio of nanorods is usually used for obtaining the birefringence effect, here we only focus on the influence of nanorod’s height h to its transfer efficiency η_{TR} and image quality of hologram. Figure 6b displays the transfer efficiency of

c-silicon and a-silicon as a function of height h , with its illuminating wavelength taken at 633 nm, for example. For c-silicon, its transfer efficiency is very sensitive to h due to the resonance of electric and magnetic dipoles in silicon [46–48] and it is capable of obtaining a high value if both orthogonal components (i.e., E_x and E_y) of incident circular polarization have high transmission and a phase difference of π , which is verified by the cases with $350 \text{ nm} < h < 440 \text{ nm}$ in Figs. 6b and c. In comparison, owing to its larger extinction coefficient, a-silicon has a much smaller transfer efficiency with an h dependence, having a maximum value at $h = 350 \text{ nm}$.

For a better understanding of the role of the resonance mode in spin photon manipulation, both cross-sectional intensity and vector profiles of electric and magnetic fields in a 370-nm thick nanorod (i.e., point A in Fig. 6b) are plotted in Fig. 6d, where two modes exist. It is noticed that the magnetic energies of both modes are highly confined in silicon nanorods. The resonance mode is dominated by a magnetic dipolar mode under x -polarized illumination but by a magnetic quadrupolar mode under y -polarized illumination [49]. As a control case for a better comparison, we also provide the relative intensity and vector profiles of electric and magnetic fields in amorphous silicon nanorods in Fig. S3 of Supporting Information. This also shows a similar magnetic resonance, while the magnitudes of electric and magnetic fields are much lower due to the higher extinction coefficient of amorphous silicon. Therefore, in our proposed silicon metasurface platform, the magnetic resonance greatly contributes to the high transmissions of both components and their phase difference of π in the simulation.

Figure 6e shows the simulated relative noise c (with $\beta = 10^{-2}$ for example) of a-silicon and c-silicon nanorods by varying the height h . The relative noise of c-silicon is small enough (below 0.5) so as to give a good quality from $h = 100 \text{ nm}$ to $h = 500 \text{ nm}$, while a-silicon fails around $h = 200 \text{ nm}$ with $c > 2$. Therefore, the ohmic loss of material is more crucial than the nanorod geometry in enhancing the holographic image quality.

Interestingly, we also note that the image quality is still satisfactory even without a polarization analyzer (i.e., removing QWP₂ and LP₂ in Fig. 2d, and $\beta = 1$). Figure 6f shows that the relative noise c of c-silicon is smaller than 2 in the color region, implying a good quality image in spite of the absence of a polarization analyzer only if the ratio η_{TR}/γ is large enough. This exciting theoretical prediction provides the fundamental proof for integrating these silicon-based metadevices directly into silicon-photonics system (e.g., waveguide, fiber) without any requirement of auxiliary devices such as polarization analyzers.

4. Conclusions and outlook

In summary, we have demonstrated a silicon metahologram for three-dimensional and broadband manipulation of spin

light at visible wavelengths from 480 nm to 680 nm. The transmission hologram imparts dispersion-less geometric phase to transmitted light in the opposite spin by spatial control of the nanorod orientation. We predict that its performance in optical efficiency and image quality can be further improved by using crystalline silicon over the amorphous silicon used in the current experiment. The metahologram-enabled spin Hall effect of light could open up new opportunities for complex manipulation of spin photons by developing novel spin-dependent metadevices in spin photonics. The developed theory describing the diffraction propagation of light in real experiment is suitable for general metasurface-based nanodevices or optical systems and suggests a straightforward physical variable of relative-noise to evaluate holographic quality. More importantly, this theory also provides evidence that all silicon-based metadevices can be integrated directly into silicon photonic circuits without the need for other additional components nor sacrifice in performance, which paves a solid path towards the application of metamaterials in photonic integrated circuits.

Supporting Information

Additional supporting information may be found in the online version of this article at the publisher's website.

Acknowledgements. This research is supported by the National Research Foundation, Prime Minister's Office, Singapore under its Competitive Research Program (CRP Award No. NRF-CRP10-2012-04). C.-W. Q., J. T., H. L. and K. H. acknowledges the support by the Agency for Science, Technology and Research (A*STAR) under BEP grant number 1521480031 (R-263-000-B88-305). H. Z. acknowledges the support of the National Natural Science Foundation of China under Grant 61205052. C.-W.Q. would like to acknowledge the support of the National Natural Science Foundation of China under Grant 61571186, via the administration of the NUS-Suzhou Institute (Grant No. R-2015-S-01). The work is partially supported by the Institute of Materials Research and Engineering and the Agency for Science, Technology and Research (A*STAR) under Grant 1021740172. Z. D. and J. Y. would like to acknowledge the funding support from the Agency for Science, Technology and Research (A*STAR) Young Investigatorship (grant number 0926030138), SERC (grant number 092154099), and the National Research Foundation grant award No. NRF-CRP 8-2011-07.

Authors contributions. K. H., L. Z., S. M. and C. Q. conceived the idea. K. H., S. M., and C. Q. carried out simulation, the structural design, and discussion on the data analysis. Z. D. and J. Y. fabricated the samples. Y. L. measured the refractive index of the samples. K. H., H. L. and J. T. implemented the experimental characterization. K. H., Z. D., L. Z., J. T., J. Y. and C. Q. prepared the manuscript. J. Y. and C. Q. supervised the overall work. All the authors analyzed the data and discussed the results.

Received: 9 December 2015, **Revised:** 7 March 2016,

Accepted: 8 March 2016

Published online: 15 April 2016

Key words: metasurface, dielectrics, holography, nanophotonics.

References

- [1] N. Yu, P. Genevet, M. A. Kats, F. Aieta, J. Tetienne, F. Capasso, and Z. Gaburro, *Science* **334**, 333 (2011).
- [2] L. Liu, X. Zhang, M. Kenney, X. Su, N. Xu, C. Ouyang, Y. Shi, J. Han, W. Zhang, and S. Zhang, *Adv. Mater.* **26**, 5031 (2014).
- [3] S. Sun, Q. He, S. Xiao, Q. Xu, X. Li, and L. Zhou, *Nature Mater.* **11**, 426 (2012).
- [4] F. Aieta, P. Genevet, M. A. Kat, N. Yu, R. Blanchard, Z. Gaburro, and F. Capasso, *Nano Lett.* **12**, 4932 (2012).
- [5] X. Chen, L. Huang, H. Muhlenbernd, G. Li, B. Bai, Q. Tan, G. Jin, C. Qiu, S. Zhang, and T. Zentgraf, *Nature Commun.* **3**, 1198 (2012).
- [6] P. Genevet, N. Yu, F. Aieta, J. Lin, M. A. Kats, R. Blanchard, M. O. Scully, Z. Gaburro, and F. Capasso, *Appl. Phys. Lett.* **100**, 013101 (2012).
- [7] M. Q. Mehmood, S. Mei, S. Hussain, K. Huang, S. Y. Siew, L. Zhang, T. Zhang, X. Ling, H. Liu, J. Teng, A. Danner, S. Zhang, and C. Qiu, *Adv. Mater.* DOI: 10.1002/adma.201504532 (2016).
- [8] G. Li, M. Kang, S. Chen, S. Zhang, E. Pun, K. Cheah, and J. Li, *Nano Lett.* **13**, 4148–4151 (2013).
- [9] K. Huang, H. Liu, F. J. Garcia-Vidal, M. Hong, B. Luk'yanchuk, J. Teng, and C. Qiu, *Nature Commun.* **6**, 7059 (2015).
- [10] X. Ni, A. V. Kildishev, and V. M. Shalaev, *Nature Commun.* **4**, 2807 (2014).
- [11] L. Huang, X. Chen, H. Muhlenbernd, H. Zhang, S. Chen, B. Bai, Q. Tan, G. Jin, K. Cheah, C. Qiu, J. Li, T. Zentgraf, and S. Zhang, *Nature Commun.* **4**, 2808 (2013).
- [12] G. Zheng, H. Muhlenbernd, M. Kenney, G. Li, T. Zentgraf, and S. Zhang, *Nature Nanotech.* **10**, 308 (2015).
- [13] Y. W. Huang, W. Chen, W. Tsai, P. Wu, C. Wang, G. Sun, and D. Tsai, *Nano Lett.* **15**, 3122 (2015).
- [14] W. T. Chen, K. Yang, C. Wang, Y. Huang, G. Sun, I. Chiang, C. Liao, W. Hsu, H. Lin, S. Sun, L. Zhou, A. Liu, and D. Tsai, *Nano Lett.* **14**, 225 (2013).
- [15] B. Walther, C. Helgert, C. Rockstuhl, F. Setzpfandt, F. Eilenberger, E. Kley, F. Lederer, A. Tunnermann, and T. Pertsch, *Adv. Mater.* **24**, 6300 (2012).
- [16] Y. Montelongo, J. Tenorio-Pearl, C. Williams, S. Zhang, W. Milne, and D. Wilkinson, *Proc. Natl Acad. Sci. USA* **111**, 12679 (2014).
- [17] Y. Montelongo, J. Tenorio-Pearl, W. Milne, and T. Wilkinson, *Nano Lett.* **14**, 294 (2013).
- [18] L. Huang, H. Muhlenbernd, X. Li, X. Song, B. Bai, Y. Wang, and T. Zentgraf, *Adv. Mater.* DOI: 10.1002/adma.201502541 (2015).
- [19] D. Wen, F. Yue, G. Li, G. Zheng, K. Chan, S. Chen, M. Chen, K. Li, P. Wong, K. Cheah, E. Pun, S. Zhang, and X. Chen, *Nature Commun.* **6**, 8241 (2015).
- [20] G. Li, S. Chen, N. Pholchai, B. Reineke, P. Wong, E. Pun, K. Cheah, T. Zentgraf, and S. Zhang, *Nature Mater.* **14**, 607 (2015).
- [21] N. Segal, S. Keren-Zur, N. Hendler, and T. Ellenbogen, *Nature Photon.* **9**, 180 (2015).
- [22] C. Barsi, W. Wan, and J. W. Fleischer, *Nature Photon.* **3**, 211 (2009).
- [23] A. Jesacher, S. Bernet, and M. Ritsch-Marte, *Opt. Exp.* **22**, 20530 (2014).
- [24] J. Moran, *Appl. Opt.* **10**, 412 (1971).
- [25] J. E. Curtis, B. A. Koss, and D. G. Grier, *Opt. Commun.* **207**, 169 (2002).
- [26] J. Cordingley, *Appl. Opt.* **32**, 2538 (1993).
- [27] K. Huang, H. Gao, G. Cao, P. Shi, X. Zhang, and Y. Li, *Appl. Opt.* **51**, 5149 (2012).
- [28] J. Arlt, K. Dholakia, L. Allen, and M. J. Padgett, *J. Mod. Opt.* **45**, 1231 (1998).
- [29] W. Chao, B. Harteneck, J. Liddle, E. Anderson, and D. Attwood, *Nature* **435**, 1210 (2005).
- [30] D. B. Williams and C. B. Carter, *The Transmission Electron Microscope*. (Springer 1996).
- [31] D. Lin, P. Fan, E. Hasman, and M. Brongersma, *Science* **18**, 298 (2014).
- [32] Y. Yang, W. Wang, P. Moitra, I. Kravchenko, D. Briggs, and J. Valentine, *Nano Lett.* **14**, 1394 (2014).
- [33] A. Arbabi, Y. Horie, M. Bagheri, and A. Faraon, *Nature Nanotech.* **10**, 937–943 (2015).
- [34] N. Shitrit, I. Yulevich, E. Maguid, D. Ozeri, D. Veksler, V. Kleiner, and E. Hasman, *Science* **340**, 724 (2013).
- [35] M. Khorasaninejad and K. B. Crozier, *Nature Commun.* **5**, 5386 (2014).
- [36] X. Ling, X. Zhou, X. Yi, W. Shu, Y. Liu, S. Chen, H. Luo, S. Wen, and D. Fan, *Light Sci. Appl.* **4**, e290 (2015).
- [37] J. Lin, J. Mueller, Q. Wang, G. Yuan, N. Antoniou, X. Yuan, and F. Capasso, *Science* **340**, 331 (2013).
- [38] J. Gotte, W. Löffler, and M. Dennis, *Phys. Rev. Lett.* **112**, 233901 (2014).
- [39] X. Yin, Z. Ye, J. Rho, Y. Wang, and X. Zhang, *Science* **339**, 1405 (2013).
- [40] L. Huang, X. Chen, H. Muhlenbernd, G. Li, B. Bai, Q. Tan, G. Jin, K. Cheah, C. Qiu, J. Li, T. Zentgraf, and S. Zhang, *Nano Lett.* **12**, 5750 (2012).
- [41] L. Huang, X. Chen, B. Bai, Q. Tan, G. Jin, T. Zentgraf, and S. Zhang, *Light: Sci. Applic.* **2**, e70 (2013).
- [42] X. G. Deng, B. Bihari, J. Gan, F. Zhao, and R. Chen, *J. Opt. Soc. Am. A* **17**, 762 (2000).
- [43] R. Gerchber and W. Saxton, *Optik* **35**, 237 (1972).
- [44] G. Lazarev, A. Hermerschmidt, S. Kruger, and S. Osten, *LCOS Spatial Light Modulators: Trends and Applications*. (Wiley-VCH, 2012).
- [45] Z. Dong, M. Asbahi, J. Lin, D. Zhu, Y. Wang, K. Hippalgaonkar, H. Chu, W. Goh, F. Wang, Z. Huang, and J. K. W. Yang, *Nano Lett.* **15**, 5976 (2015).
- [46] M. Decker, I. Staude, M. Falkner, J. Dominguez, D. Neshev, I. Brener, T. Pertsch, and Y. Kivshar, *Adv. Opt. Mater.* **3**, 813 (2015).
- [47] Y. F. Yu, A. Zhu, R. Paniagua-Dominguez, Y. Fu, B. Luk'yanchuk, and A. Kuznetsov, *Laser Photon. Rev.* **9**, 412 (2015).

- [48] I. Staude, A. E. Miroshnichenko, M. Decker, N. T. Fofang, S. Liu, E. Gonzales, J. Dominguez, T. S. Luk, D. N. Neshev, I. Brener, and Y. Kivshar, *ACS Nano* **7**, 7824 (2013).
- [49] C. F. Bohren, and D. R. Huffman, *Absorption and Scattering of Light by Small Particles*, (John Wiley & Sons, New York 1998).
- [50] H. Butt, Y. Montelongo, T. Butler, R. Rajesekharan, Q. Dai, S. G. Shiva-Reddy, T. D. Wilkinson, and G. A. J. Amaratunga, *Adv. Mater.* **24**, OP331–OP336 (2012).
- [51] Y. Yifat, M. Eitan, Z. Iluz, Y. Hanein, A. Boag, and J. Scheuer, *Nano Lett.* **14**, 2485–2490 (2014).
- [52] F. Zhou, Y. Liu, and W. Cai, *Opt. Exp.* **21**, 4348–4354 (2013).

Supporting Information

Kun Huang^{1, 2,*}, Zhaogang Dong^{2,*}, Shengtao Mei^{1, 3,*}, Lei Zhang¹, Yanjun Liu², Hong Liu², Haibin Zhu¹, Jinghua Teng², Boris Luk'yanchuk⁴, Joel K.W. Yang^{2,5,†}, and Cheng-Wei Qiu^{1,3†}

¹Department of Electrical and Computer Engineering, National University of Singapore, 4 Engineering Drive 3, Singapore 117583, Singapore

²Institute of Materials Research and Engineering, Agency for Science, Technology and Research, 2 Fusionopolis Way, Innovis, #08-03, Singapore 138634, Singapore

³NUS Graduate School for Integrative Sciences and Engineering, National University of Singapore, 28 Medical Drive, Singapore 117456

⁴Data Storage Institute, Agency for Science, Technology and Research, 2 Fusionopolis Way, Innovis, #08-01,, Singapore 138634, Singapore

⁵Singapore University of Technology and Design, 8 Somapah Road, Singapore 487372

* These authors contributed equally to this work

†Correspondence and requests for materials should be addressed to C. Q. (email: eleqc@nus.edu.sg) or J. Y. (email: yangkwj@imre.a-star.edu.sg).

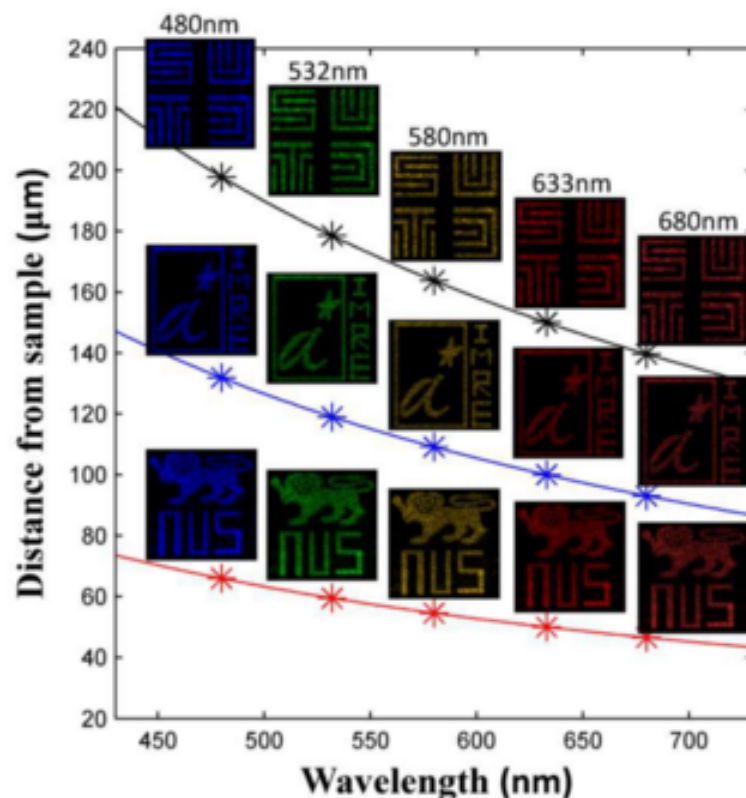


Figure S1| Simulation for broadband operation of silicon meta-hologram. The theoretical dispersion of hologram are provided by the distance between sample and the z-position of every holographic images as a function of wavelength λ . The simulation is carried out by using Eq. (3) of main text. Insets: the simulated holographic images are provided with different wavelengths of 480nm, 532nm, 580nm, 633nm and 680nm.

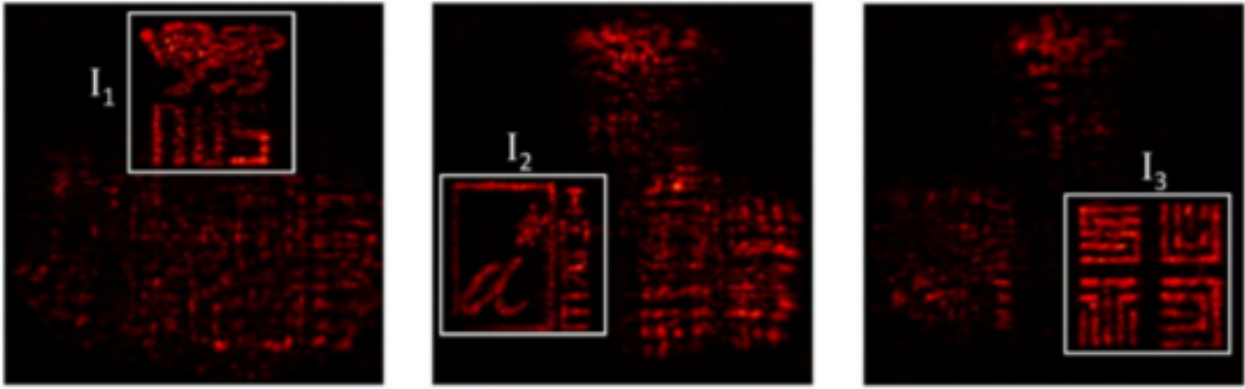


Figure S2| Calculating optical efficiency η of our silicon meta-hologram. The optical efficiency η is defined as the ratio of total intensity of three holographic images to incident intensity. For every holographic image, its intensity I_n ($n=1, 2$ and 3) is evaluated by the encircled intensity in a white square region with the size of $40\mu\text{m} \times 40\mu\text{m}$. Therefore, optical efficiency of our meta-hologram is

$$\eta = \left(\sum_{n=1}^3 I_n \right) / I_0, \text{ where } I_0 \text{ is the incident intensity.}$$

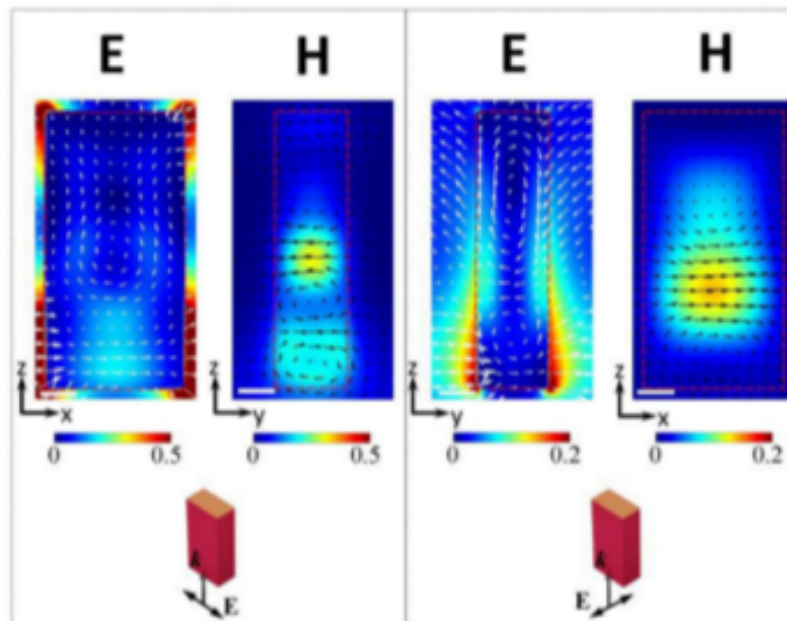


Figure S3| The cross-section intensity and vector profiles of electric (E**) and magnetic (**H**) field in our amorphous silicon nanorod (red dashed rectangles) with $h=370\text{nm}$, $w=100\text{nm}$ and $l=190\text{nm}$ under the x - (left) and y - (right) polarized illumination. All the settings in simulation are the same with Fig. 6d except the refractive index of silicon nanorod ($3.88+0.019i$ (crystalline) for Fig. 6d and $4.22+0.47i$ (amorphous) for Fig. S3). The electric and magnetic fields are normalized to those in Fig. 6d. It means that the intensity confined in amorphous silicon is much lower than that in crystalline silicon, which provides the solid proof for the low optical efficiency of our meta-hologram. The white and black arrows denote vector direction of **E** and **H**, respectively. Insets: The wave vector (k) and polarization (E) of incident light for both illuminations. Scale bar, 50nm .**

Table S1| A comparison between our silicon hologram and other reported meta-holograms.

Operating mode	Literatures	Total Efficiency	Wavelength	Twin-image	High-order diffraction	Materials
Reflection	H. Butt, et al. ⁵¹	Not reported	454nm, 532nm, 635nm	Yes	Yes	Carbon nanotube
	Y. Huang et al. ⁵²	0.64%-0.69%	405nm, 532nm, 658nm	Yes	Yes	Aluminium
	Y. Montelongo et al. ⁵³	3%	650nm	Yes	Yes	Silver
	Y. Montelongo et al. ⁵⁴	3%	405nm, 650nm	Yes	Yes	Silver
	W. Chen, et al. ⁵⁵	18%	405nm, 633nm, 780nm	Yes	Yes	Gold
	D. Wen, et al. ⁵⁶	40%	475nm-1100nm	No	No	Silver
	Y. Yifat et al. ⁵⁷	60%	1550nm	Yes	No	Gold
	G. Zheng et al. ⁵⁸	80%	600nm-1100nm	No	No	Gold
Transmission	L. Huang et al. ⁵⁹	Not reported	670nm-950nm	No	No	Gold
	B. Walther, et al. ⁵¹⁰	0.1%	905nm, 1385nm	Yes	Yes	Gold
	F. Zhou, et al. ⁵¹¹	0.2%	1550nm	Not reported	Not reported	Gold
	K. Huang, et al. ⁵¹²	2%	532nm	No	No	Chromium
	X. Ni, et al. ⁵¹³	10%	676nm	No	No	Gold
	A. Arbabi, et al. ⁵¹⁴	84%-91%	915nm	No	No	Silicon
	Our hologram	3%	480nm-680nm	No	No	Silicon

Section 1. Comparison between our meta-hologram and other reported meta-holograms

In order to give a clear demonstration of our hologram, we provide a detailed comparison between our meta-hologram and other reported holograms in optical efficiency, operating wavelength, twin-image and high-order diffraction issues in Table S1. It clearly shows that the performance of reflective meta-holograms has been improved very quickly after 2015, especially in optical efficiency, high-order diffraction and twin-image issues. However, for transmissive meta-holograms, the good performance is only shown in infrared region. The broadband operation in short-wavelength visible light is very challenging in a transmitted mode while it is realized by our silicon hologram with a bandwidth of 200nm from blue to red light. Therefore, our hologram is the first one to realize the broadband operation of visible light among all transmissive metaholograms. Although our efficiency is not high enough due to the amorphous silicon, it has the great potential in enhancing the efficiency through crystallized silicon as demonstrated in main text.

Section 2. Hologram design

The retrieval algorithm for hologram phase is based on Gerchberg-Saxton iterations. In all the numerical calculation of hologram design, the incident **circular-shape beam with axial symmetry** is assumed to be uniform with its diameter of 120 μ m, which is the same with that of

phase profile. The incident phase $P^i(x_0, y_0)$ (where $i=1, 2$ and 3 indicating three holographic

images at different z-cut planes) in i-th iteration is a weighted superposition of three phase profiles $P_n^{i-1}(x_0, y_0)$ obtained in last iteration, where $P_n^{i-1}(x_0, y_0)$ is obtained by the reverse

propagation of its real image. That is, $P^i(x_0, y_0) = \sum_{n=1}^3 \chi_n^{i-1} \cdot P_n^{i-1}(x_0, y_0)$, where the weighted

coefficients $\chi_n^{i-1} = RMS_n^{i-1} / \sum_{n=1}^3 RMS_n^{i-1}$, RMS_n^{i-1} is the root-mean-square error between real (

$I_n^{i-1}(x_n, y_n)$) and ideal ($I_n^{ideal}(x_n, y_n)$) images at every z-cut plane and can be expressed as

$$RMS_n^{i-1} = \sqrt{\left(\sum \left| I_n^{i-1} - I_n^{ideal} \right|^2 \right) / (M \times M - 1)}$$

with M being the sampling number along x or y direction in the region of interest.

References:

- [S1] Butt, H. et al. Carbon Nanotube Based High Resolution Holograms, *Adv. Mat.* **24**, OP331–OP336 (2012).
- [S2] Huang, Y. et al. Aluminum Plasmonic Multicolor Meta-Hologram, *Nano Lett.* **15**, 3122–3127(2015)
- [S3] Montelongo, Y. et al. Polarization Switchable Diffraction Based on Subwavelength Plasmonic Nanoantennas, *Nano Lett.* **14**, 294–298 (2014).
- [S4] Montelongo, Y. et al. Plasmonic nanoparticle scattering for color holograms. *Proc. Natl Acad. Sci. USA* **111**, 12679–12683 (2014).
- [S5] Chen, W. et al. High-efficiency broadband meta-hologram with polarization controlled dual images. *Nano Lett.* **13**, 225–230 (2013).
- [S6] Wen, D. et al. Helicity multiplexed broadband metasurface holograms, *Nat. Commun.* Doi: 10.1038/ncomms9241(2015).
- [S7] Yifat, Y. et al. Highly Efficient and Broadband Wide-Angle Holography Using Patch-Dipole Nanoantenna Reflectarrays, *Nano Lett.* **14**, 2485–2490 (2014).
- [S8] Zheng, G. et al. Metasurface holograms reaching 80% efficiency, *Nat. Nano.* **10**, 308–312(2015)
- [S9] Huang, L. et al. Three dimensional optical holography using a plasmonic metasurface. *Nat. Commun.* **4**, 2808 (2013).
- [S10] Walther, B. et al. Spatial and spectral light shaping with metamaterials. *Adv. Mater.* **24**, 6300–6304 (2012).
- [S11] Zhou, F. et al. Plasmonic holographic imaging with V-shaped nanoantenna array. *Opt. Express* **21**, 4348–4354 (2013).

[S12] Huang, K. et al. Ultrahigh-capacity non-periodic photon sieves operating in visible light. *Nat. Commun.* 6, 7059(2015).

[S13] Ni, X., Ishii, S., Kildishev, A. V. & Shalaev, V. M. Metasurface holograms for visible light. *Nat. Commun.* 4, 2807 (2013).

[S14] Arbabi, A. et al. Dielectric metasurfaces for complete control of phase and polarization with subwavelength spatial resolution and high transmission. *Nat. Nano.* DOI: 10.1038/NNANO.2015.186 (2015).